Observation of mixed types of energy gaps in some II–VI semiconductors nanostructured films: towards enhanced solar cell performance

E. Shalaan[1,2] · **E. Ibrahim**[2] · **F. Al-Marzouki**[1] · **M. Al-Dossari**[1,3]

Abstract

All solid-state quantum dots embedded multi-junction solar cell with the device structure of (Glass/ITO/ZnTe/ZnS/CdS/Au) is achieved to boost the photo-conversion efficiency by incorporating inner layer of ZnS and by effectively utilizing the entire solar spectrum. Electron beam evaporation was used to deposit the three semiconductor materials ZnTe, ZnS and CdS thin films. The optical properties and energy bandgap of each of the three materials were determined using ellipsometric measurements. The device performance was investigated using current voltage (J–V) techniques at room temperature and under AM1.5 illumination conditions. In this study, we showed that the optical energy gaps of some nanoscale binary semiconductor compounds from II–VI family exhibit both direct and indirect types of optical energy bandgap and there is a giant increase in their direct values.

1 Introduction

In recent years, semiconductor nanostructure materials have received much attention as crucial components for solar cell devices due to their exceptional chemical and physical properties [1–12]. Using such nanostructure with tailored bandgap-thickness ratios as the fundamental constituents is likely to play a key role in future solar cell devices due to carrier confinement within nanostructures.

Compound semiconductors consisting of elements II–VI or III–VI can be considered as the basic, effective and efficient materials in the design of energy harvesting devices that directly convert sunlight into electricity with great efficiency.

Compound semiconductors consisting of elements II–VI or III–VI can be considered as the basic, effective and efficient materials in the design of energy harvesting devices that directly convert sunlight into electricity with great efficiency. These materials are one of the most promising solutions towards mass production and efficient low-cost solar cells due to their excellent electronic properties, abundance of raw materials, deposition at low temperatures, approving with flexible substrates, and good thermal stability. Additionally, they can be used to manufacture various sizes of solar modules to cover a wide range of power generation outputs, ranging from milli-watts to mega-watts. The current international and global researches are focused to developing scalable manufacturing strategies for solar modules with the intention of realizing the maximum performance of solar energy collecting at the lowest possible cost. In recent years, it has been observed that with different size scales, there is a good improvement in efficiency but there was still an efficiency gap between small- and large-area devices. There are many challenges that remain and need more research and study [13–16].

Further reductions in the total cost of solar cells can be obtained by thin-film technology. In this way, the material consumption is minimal while maintaining cell efficiency to size ratio. There are multiple methods of preparing thin

✉ E. Shalaan
eshalaan@yahoo.com; eshalan@kau.edu.sa

1   Physics Department, Faculty of Science, King Abdulaziz University, Jeddah, Saudi Arabia

2   Physics Department, Faculty of Science, Suez Canal University, Ismailia, Egypt

3   Physics Department, Faculty of Science, King Khaled University, Jeddah, Saudi Arabia

films, however, the process itself is a complex when the layer that needs to be prepared is made up of more than one component. Co-evaporation [17, 18] and reactive sputtering [19–22] are the usual approaches for the production of multilayer solar cells. These two techniques have critical common problem that is the struggling to control the film composition over a large surface area. Electron beam evaporation is performed better in relation to film composition and quality [23–26]. All these methods require vacuum to operate. The non-vacuum deposition techniques including electrodeposition [27–29], electroplating [30, 31] and chemical bath deposition [32–34] are well-established methods in the photovoltaic industry.

CdTe-based solar cells have gained much interest in the past decades due to their suitability in photovoltaic applications [35–41]. The obtained efficiency slowly increased from 15 to 21%. This value of efficiency is still far away from the theoretical limits of solar cell efficiency [42, 43]. The reduction in the solar cell efficiency is mainly caused by non-uniformity of one or more of the different layers within the structure. To exceed the maximum current value of device efficiency, some researchers suggested that the thickness of CdS layer should be reduced because of the high absorption coefficient of CdS materials. Thin films of cadmium sulfide CdS are widely used as a buffer layer in high-efficiency solar cells. The high absorption coefficient of CdS prevents much amount of solar radiation from reaching the CdTe layer in ITO/CdS/CdTe-based solar cells. Subsequently, much of the charge carriers generated at the ITO/CdS interface are blocked and do not move toward the depletion region resulting in a decrease in the short-circuit current density. The possible solution is the decreasing of the thickness of CdS layer. Nevertheless, the small thickness of CdS layer may lead to a device failure due to the direct contact between CdTe and ITO if some pinholes were present. These pinholes are largely formed in small thickness layers (below 100 nm). Pinholes create undesirable shunt paths within the device. Thus, the overall performance of the device will be reduced. The conceivable solution for pinholes related problem is building thicker device. But thicker device will produce smaller current density (Jsc) due to the recombination current caused by the absorption which in turn greatly affects the output power efficiency [44–49]. One thinkable solution, to use a thin CdS layer without its drawback's effects, is use of a nanoparticle route. Small sizes of these nanoparticles will avoid the formation of pinhole and fill any space that can be created during growth process. Therefore, using nanoparticle CdS thin film with small thickness may override this problem. The small particle size prevents the formation of undesired pinholes.

Semiconductor nanostructure quantum dots based on II–VI group, such as CdSe, ZnS, ZnTe and CdTe, have high absorption coefficient and tunable bandgap energy which make them very suitable materials for solar cell devices [50–52].

In the present work, nanoscale(n)-CdS/(n)-ZnS thin films were used as a combined N-type layer for spectral tuning and modifying the energy levels resulted in a more efficient solar cell. The required P-type material for the current cell configuration is (n)-ZnTe. As ZnS bandgap is relatively wide 3.5 eV, it allows more photons from short wavelength regime to pass through it.

To enhance solar efficiency and to improve the device parameters, the following device structure was fabricated glass/ITO/ZnTe/ZnS/CdS/Au. Here, ZnTe is used as absorber layer, ZnS is utilized as a buffer layer and finally CdS is used as optical window layer. Further modification also applied by reduction of CdS layer. Thin-film solar cells have been intensively developed to reduce the production cost of the photovoltaic (PV) modules. This goal also is achieved here, in fact, all layers are below 200 nm, and the whole device thickness is typically below 800 mm.

1.1 Experimental details

Nanostructured ZnTe, ZnS and CdS thin films have been deposited on glass substrates by electron beam evaporation system, model NEE-4000, Nano-Master, Inc., USA. When the base pressure reached 1×10^{-6} mbar, the electron beam was initiated and then manipulated at the following conditions: ($V = 8$ kV, $I = 300$ mA). Stoichiometric powders of each compound (99.999%) were used as source materials in graphite crucible. For all deposition processes, the substrate temperature was kept constant at 300 K.

For building solar cell device, ZnTe layer (about 120 nm) was deposited on ITO-coated glass substrate, followed by deposition of ZnS (200 nm) and finally, CdS (200 nm) was deposited as a top layer. After that, gold (30 nm) electrode was deposited through an Al mask with a separate cell area of 0.09 cm^2.

The morphologies and structure properties of samples were characterized by atomic force microscopy (Omicron VT, Germany) and by X-ray powder diffractometer (Rigaku Ultima IV, Japan) using CuK$_{\alpha 1}$ radiation ($\lambda = 1.54056$ Å) operating at 40 kV with scanning range from $2\theta = 5°$–$90°$. Optical study was carried out by spectroscopic ellipsometry in the wavelength range from 192 to 1700 nm. Ellipsometric measurement data were collected using M-2000 ellipsometer, J. A. Woollam, USA.

Performance of ITO/ZnTe/ZnS/CdS/Au solar cell was characterized by J–V curve using semiconductor characterization system model 4200-SCS, Keithley, USA. The cell efficiency was measured under Air Mass 1.5G solar irradiations with 100 mW/cm^2 illumination power using Oriel xenon arc lamp controlled by power supply model 69931,

Newport Inc., USA. The intensity of illuminated light was calibrated with a standard reference cell.

2 Results and discussion

Figure 1 shows the XRD patterns of the deposited ZnTe, ZnTe/ZnS and ZnTe/ZnS/CdS thin-film samples. This figure reveals that all samples have broad humps indicating amorphous/nanocrystal structure. Additionally, the XRD pattern of ZnTe/ZnS/CdS thin-film multilayer sample shows very small peaks at $2\theta = 24.8°$, 26.5° and 28.18° which correspond to the lattice planes (100), (002) and (101), respectively. The observed short peaks could be attributed to a short-range order within the nanostructure. The analyses of these peaks suggest that this sample has hexagonal structure in confirmation with JCPDS (41-1049).

However, this XRD analysis does not fully evaluate the crystal structure of the ZnTe/ZnS/CdS thin-film multilayer sample. A more detailed account of the structure is given by AFM investigation. AFM is always a crucial tool, especially when it comes to the height and particle size measurements of a nanoscale sample. Here, topography images of 20×20 μm² were captured in contact mode with controlling the scanning velocity to optimize the noise level in the images. Figure 2a, b shows the surface topography of the ZnTe/ZnS/ CdS thin-film multilayer sample in 2D and 3D, respectively.

During AFM acquisition process, some different regions were selected where no obvious concavities or crests were present to avoid a simulated bias of the results. Furthermore, the obtained parameters (particle height and particle diameter) were averaged over different surface images. The obtained parameters are illustrated in Fig. 3a, b. Both parameters reveal a nanostructure nature of the sample with the mean height of 8.6 nm and the mean diameter of about 51 nm.

It is believed that a better study would first examine an optical property of each individual layer that constitutes the whole device before characterizing the device itself. This will help for obtaining useful information and aid in interpreting the device properties. Figure 4 shows the spectroscopic ellipsometry measurements data (lines) and model (short dots) for angles of incidence of 45°, 50° and 55° for ZnTe, ZnS and CdS thin films deposited on glass substrates using electron beam evaporation technique.

The accuracy of ellipsometry for the determination of ultra-thin-film thicknesses as well as optical properties is very high and precise. The only major drawback of ellipsometry is that to deduce the required properties, the measured data should be fitted to some suitable functions. Perhaps the most serious disadvantage of ellipsometry is the fitting process.

However, there are several other important limitations. For example, the small size of the incident beam leads to low spatial resolutions, the accuracy issue for film thickness determination below 10 nm and the depolarization that arises from surface roughness or non-uniformity of the thin film. Fortunately, the new advanced ellipsometer overrides these limitations. Here, the optical properties were measured using M-2000 ellipsometer, J. A. Woollam, USA. This

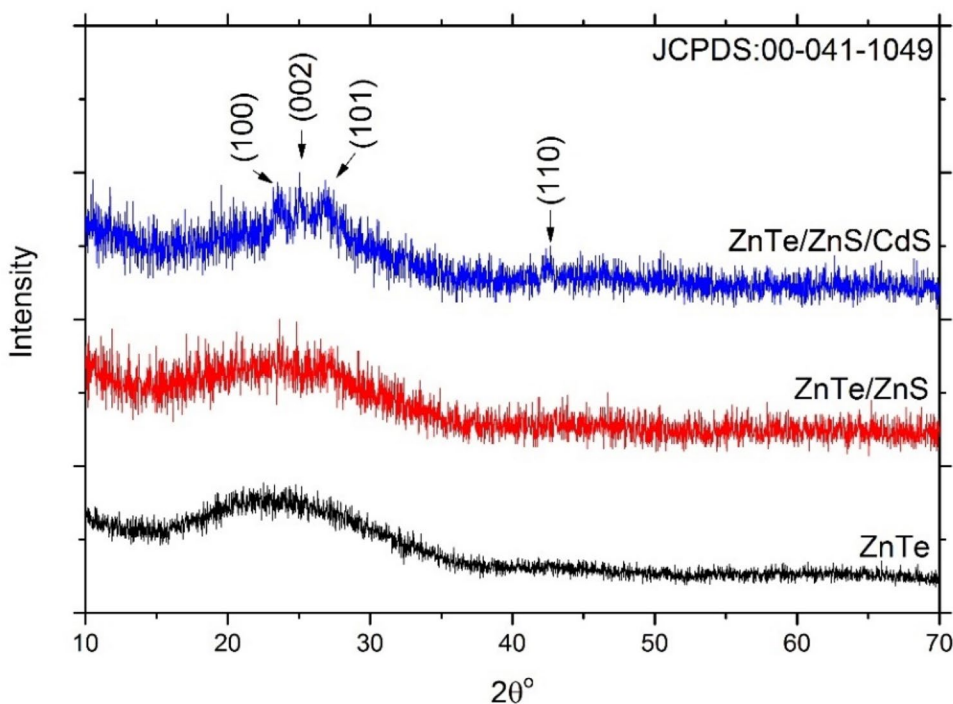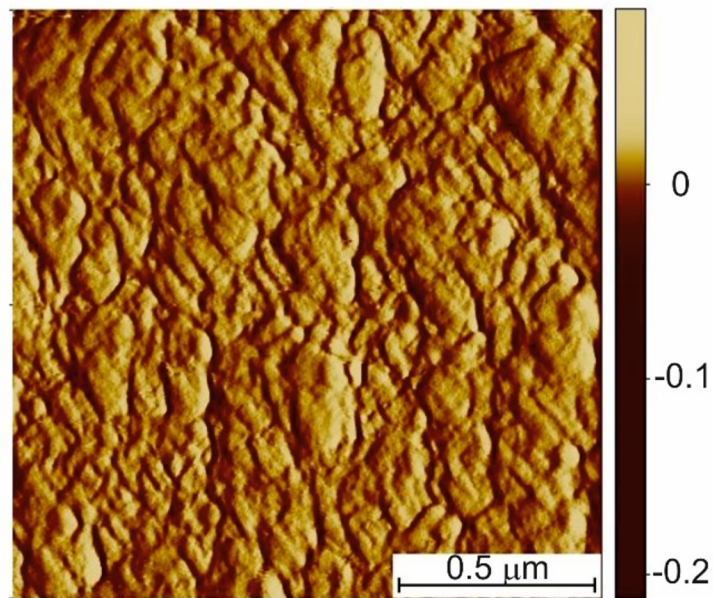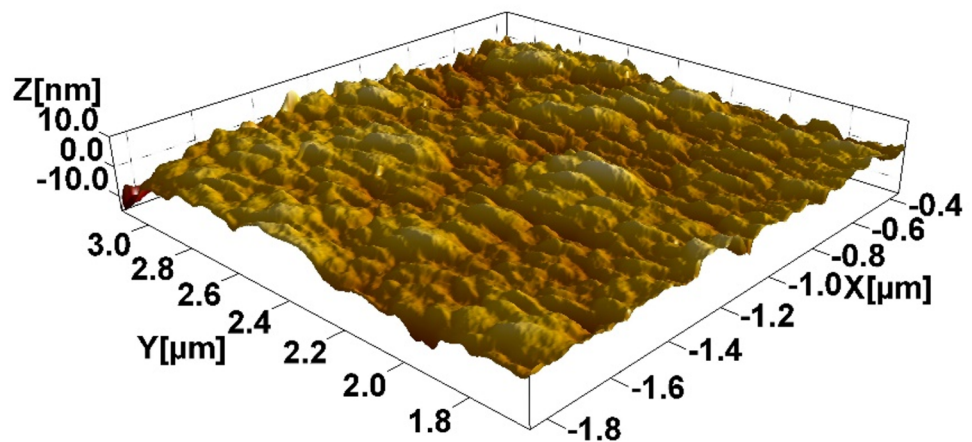**Fig. 1** Typical XRD patterns of ZnTe, ZnTe/ZnS and ZnTe/ZnS/ CdS thin-film samples

(a)

(b)

system incorporates a continuously rotating compensator before the sample to eliminate the depolarization. The presence of high-speed CCD detection makes it possible to collect the entire spectrum from 193 to 1700 nm in just 2 s. This fast recoding permits to obtain a large-area uniformity mapping. This configuration eliminates the effect of small size limit of incidence light. Moreover, the accuracy of the phase change detection enhanced the sensitivity of the ellipsometer to any surface layers within a small fraction of a nanometer [53–55].

As shown in the Fig. 4, it is clear that an excellent fit was achieved for all samples. To increase the accuracy of the results, the transmission spectra were included into the calculations. Figure 5 shows the measured and calculated/generated transmission spectra of all samples.

Figure 6 shows the obtained refractive index and extinction coefficient of ZnTe, ZnS and CdS thin films. These two figures show normal behavior. The extinction coefficient k is related to the absorption coefficient by $\alpha = 4\pi k/\lambda$, where α is the absorption coefficient and λ is the wavelength. Traditionally, a classic and well-known method for deducing the energy gaps of materials is usually carried out through Tauc's approach [56]. The benefit of this approach is that the calculation procedures are very simple and straightforward. Based on Tauc's equation, $(\alpha h\upsilon)^2$ versus $(h\upsilon)$ plot shows a straight line. The extrapolation of this straight line will

Fig. 3 **a** Particle diameter distributions of the ZnTe/ZnS/CdS thin-film multilayer sample. **b** Particle height distributions of the ZnTe/ZnS/CdS thin-film multilayer sample

(a)

(b)
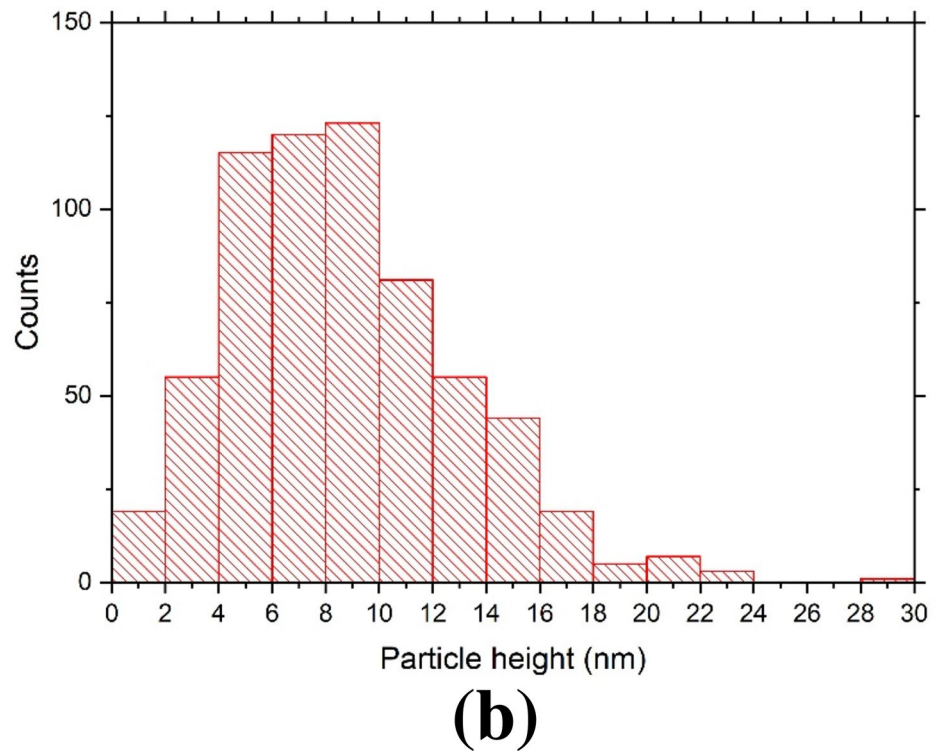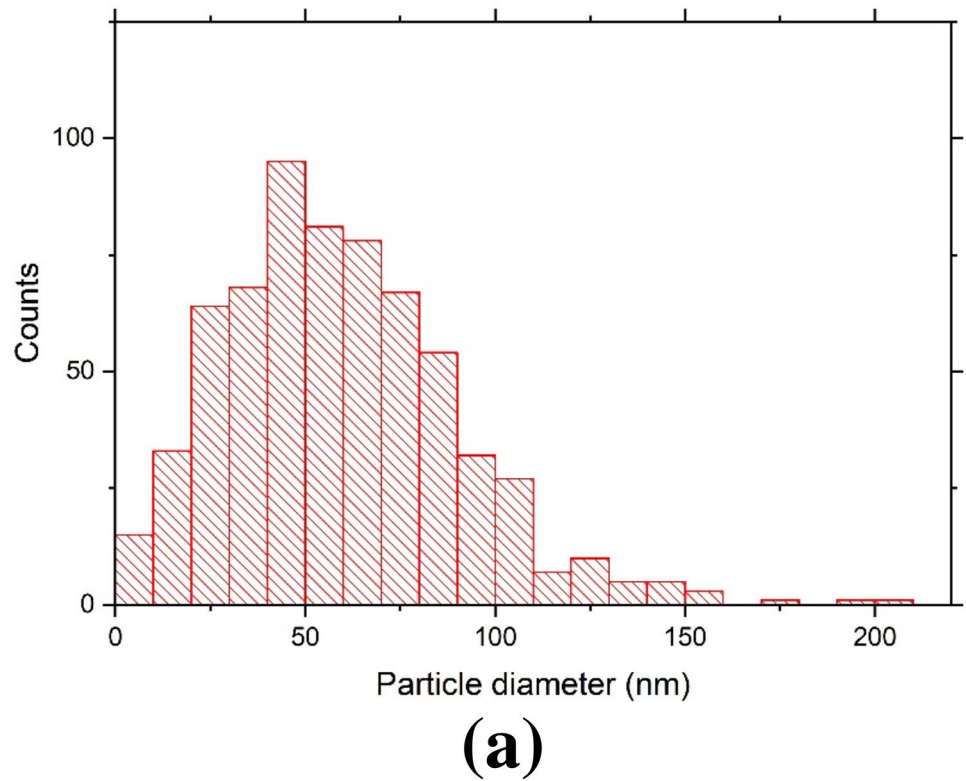
intercept the *x*-axis at the direct energy gap value. While a plotting of $(\alpha h\upsilon)^{1/2}$ versus $(h\upsilon)$ gives the indirect optical energy gap.

The results obtained from the Tauc's calculations are shown in Fig. 7. As can be seen from this figure, there is a clear trend of increasing direct energy gaps of the thin-film

Fig. 4 Ellipsometric parameters (ψ, Δ) for ZnTe, ZnS and CdS films
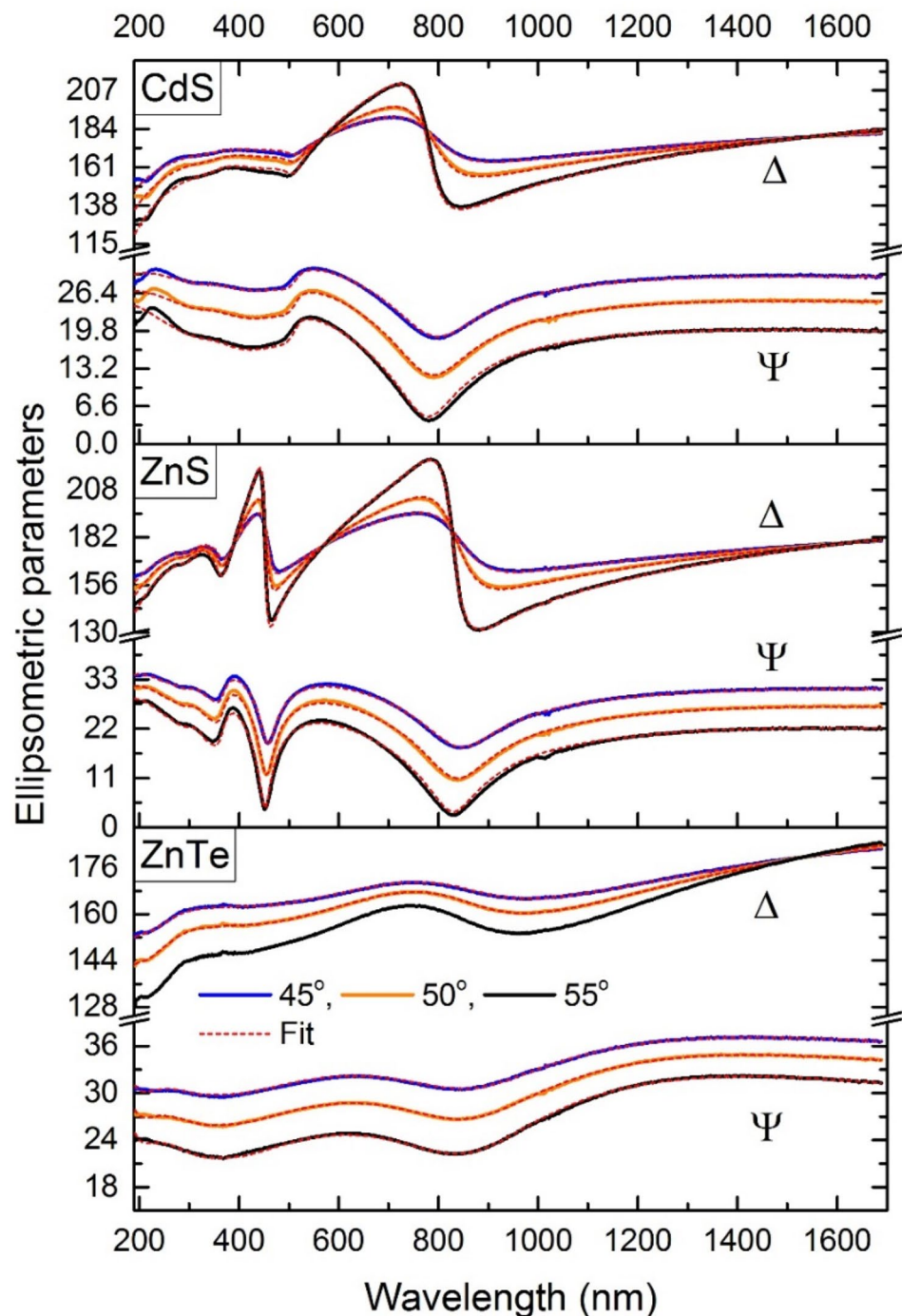
samples in comparison to their bulk counterpart materials. The differences between the calculated energy gaps of the thin-film samples and bulk materials are highlighted in Table 1.

The observed increase in energy gaps could be attributed to the nanoscale nature of the thin-film samples. It is necessary here to clarify exactly this fact. To determine the effects of size on the energy gap, the Brus equation was utilized and employed to calculate the particle size of the samples. The

first theoretical calculation for CdS nanoparticles was performed by Brus. He assumed that the particle has a spherical shape and has obeyed the following relation [57, 58]:

$$E_g^{Nano} = E_g^{Bulk} + \frac{h^2}{8R^2}\left(\frac{1}{m_e^*} + \frac{1}{m_h^*}\right) - \frac{1.8e^2}{4\pi\varepsilon\varepsilon_o R},$$

where, E_g^{Nano} is the energy gap of nanoscale thin-film sample, E_g^{Bulk} is the energy gap of their corresponding bulk

Fig. 5 Measured and generated optical transmission spectra of ZnTe, ZnS and CdS thin films
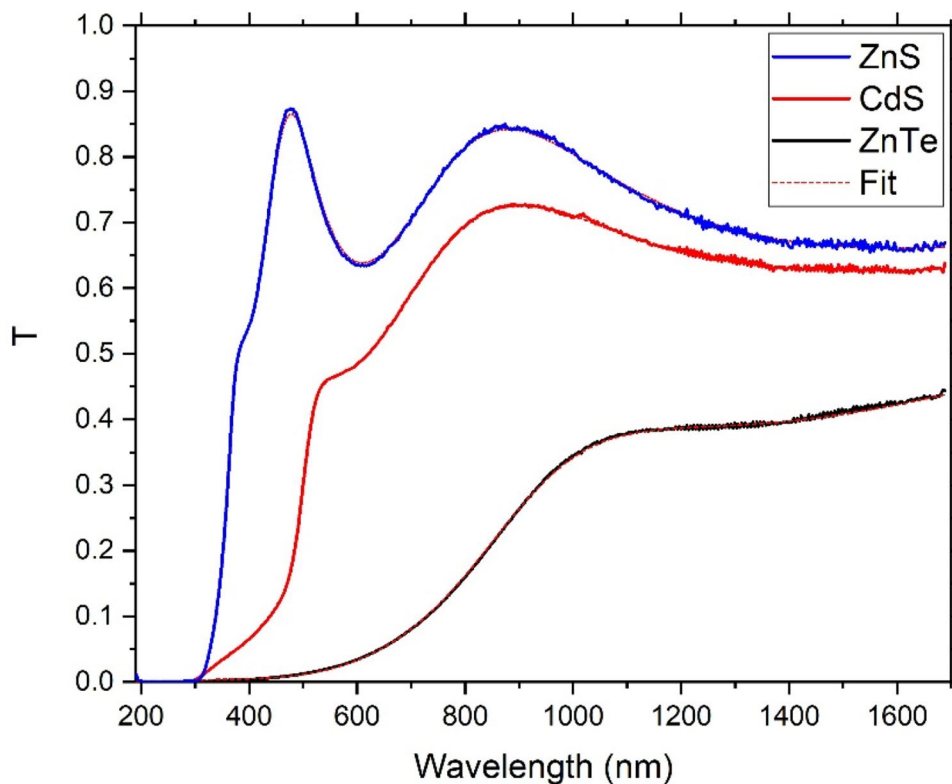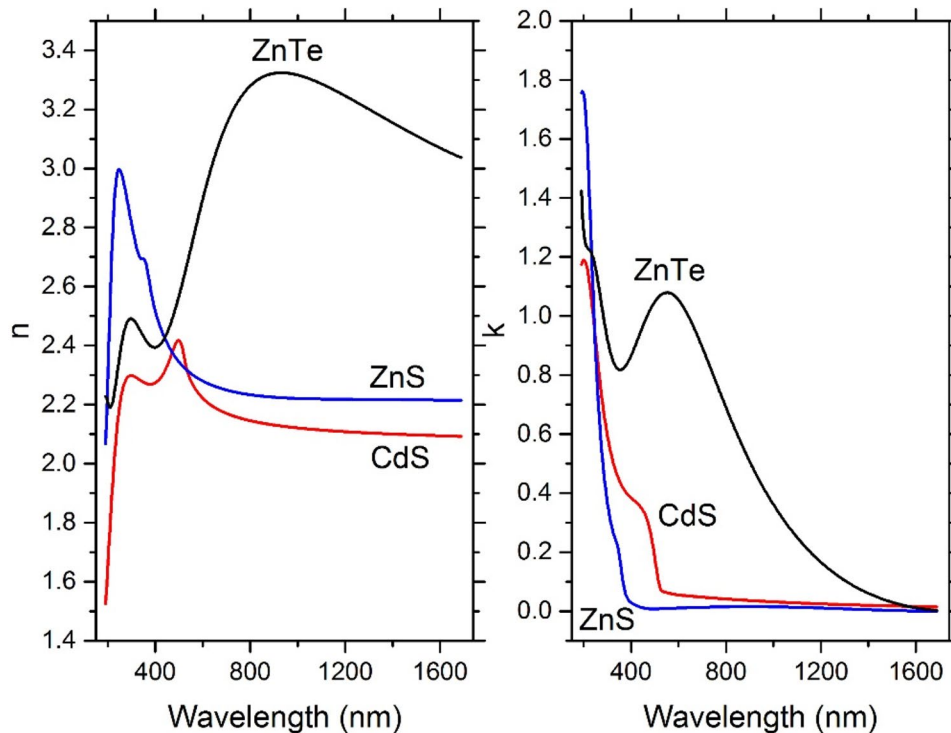

Fig. 6 Refractive index and extinction coefficient of ZnTe, ZnS and CdS thin films

material and *R* is the radius of the nanoparticle in meters. The other symbols have their usual meaning. To deduce the particle diameter of nanoscale thin-film samples, the Brus equation was used. The obtained values of the particle diameters are summarized in Table 1. These values are found to be around 2–3 nm which are typical size for

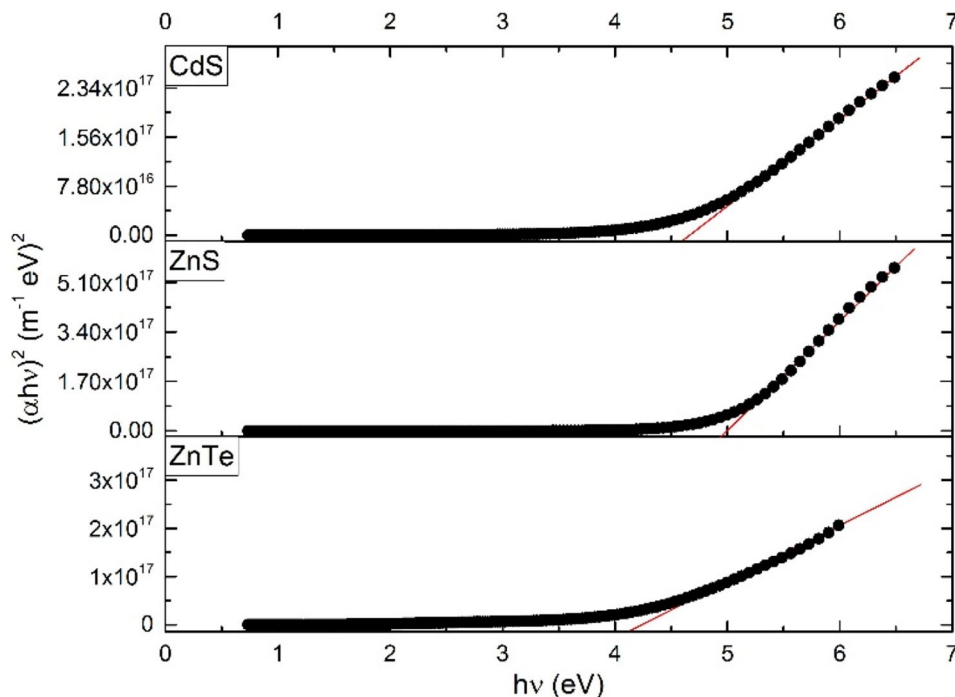**Fig. 7** Tauc's plots for CdS, ZnS and ZnTe thin films

Table 1 Lattice parameters and direct optical energy gap for CdS, ZnS and ZnTe thin films

	Structure	Lattice parameters	Type	E_g^{bulk} (eV)	E_g^{nano} (eV)	m_e^*	m_h^*	$D\ (=2R)$ (nm)
CdS	c	0.582	n-type	2.42	4.69	0.21	0.8	2
	h	0.414, 0.675		2.5				
ZnS	c	0.541	n-type	3.54	4.86	0.25	0.6	3
	h	0.381, 0.623	p-type	3.67				
ZnTe	c	0.610	p-type	2.39	4.18	0.2	0.2	2.8
	h	0.427, 0.699						

c (cubic: zinc blende), h (hexagonal: wurtzite)

quantum dots. To confirm these results, an AFM investigation for CdS, ZnS and ZnTe thin films has been performed. Typical surface topography for these films is illustrated in Fig. 8.

AFM analysis reveals that the particle sizes for CdS, ZnS and ZnTe are 59, 36 and 42 nm, respectively. These results are not consistent with data obtained from Brus equation. However, both results for particle diameter values are still in nanoscale range. The optical energy gaps obtained from ellipsometric measurements are considered very accurate. The necessary condition for such values is that the particle size of the materials should be very small (around 3 nm). But the particle size obtained from AFM analysis is different by large value. The possible explanation for such inconsistency could be attributed to the presence of quantum dots embedded in the materials. Closer look at AFM image of CdS sample, for example, confirms this fact, (Fig. 8: top left). These results suggested that the presence of indirect energy gap should be also investigated. Figure 9 shows the Tauc's plots for the indirect energy gaps of the thin-film samples.

All CdS, ZnS and ZnTe thin-film samples exhibit single or multiple indirect transitions. In principle, semiconductor materials may have direct or indirect bandgap depending upon their crystal structures. According to Tauc, crystalline materials are favorite to have direct energy gap, on the other hand, indirect nature of transition is more likely to happen in non-crystalline materials. In some cases, when the material is partially crystalline, both types of transition may be present. In our study, we have suggested that the structure of the prepared films are quantum dots embedded nanocrystalline materials. It is possible, therefore, that these films could exhibit both direct and indirect energy gaps. Figure 10 summarizes the obtained energy gap types and values for these films.

The main design parameters for solar cells are the bandgap energy and the minority carrier diffusion length. The bandgap determines at which point in the solar spectrum the semiconductor starts absorbing light, while the minority carrier diffusion length determines how far minority carriers diffuse before recombining. It is very
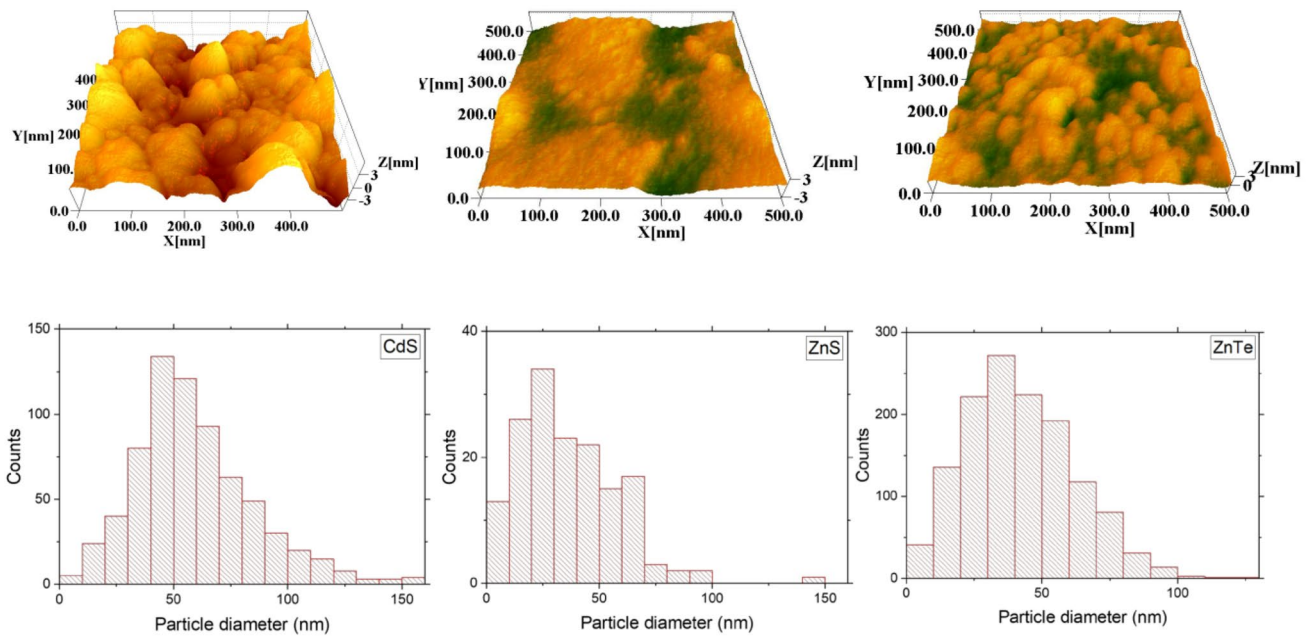
Fig. 8 AFM topographic images of CdS, ZnS and ZnTe thin films (top) and particle size distributions (bottom)
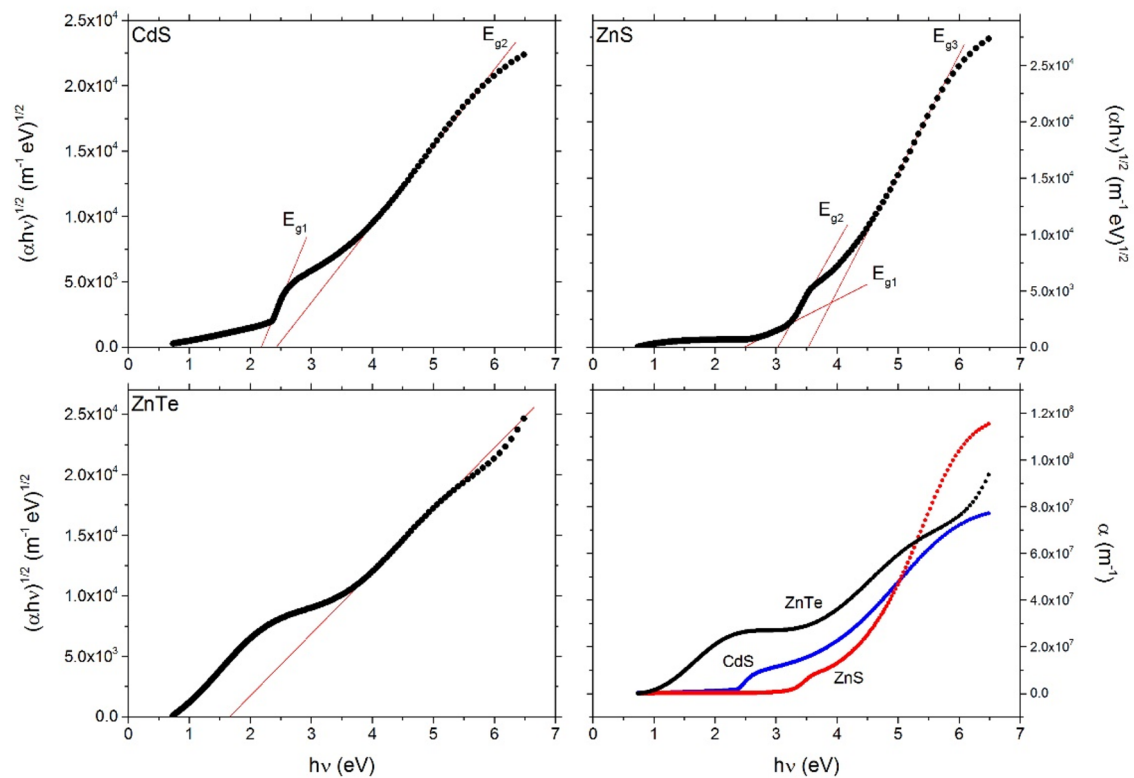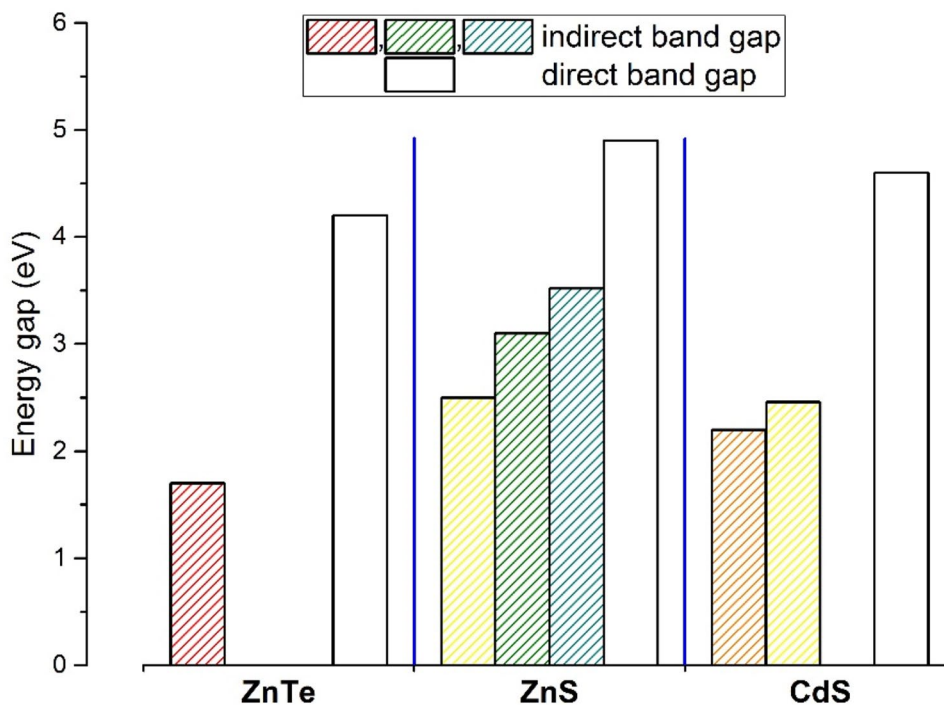

Fig. 9 Indirect energy bandgaps plots for CdS, ZnS and ZnTe thin films

Fig. 10 Energy bandgap types of CdS, ZnS and ZnTe thin films

important that the photo-generated minority carriers have to cross the junction before they recombine. Direct bandgap materials have strong optical transitions between the valence and conduction band. However, indirect materials have fairly weak optical transitions. This is because absorption and emission of a photon must occur with the simultaneous absorption or emission of a phonon. In solar cell design, thicker thickness is usually required for absorbing most of incident photons. Unfortunately, thicker thickness affects negatively the efficiency because of the minority carrier diffusion length. Generally, the minority diffusion length of carriers in indirect materials is very long, while it is very short in most direct materials. Therefore, a brilliant choice of materials that exhibit direct and indirect energy gaps as well as some localized energy levels to assist photon absorption and charge generation is very important. Additionally, the energy band diagram of the whole device should be engineered to permit these features and prevent charge recombination.

In the light of the above discussion, we proposed solar cell device structure as described in Fig. 11 to achieve a good balance between thickness, bandgap, absorption and carrier collection. The presence of quantum dots made a localized energy levels within the sample. The big direct gap permits the absorption of IR radiation, this thermal energy assists the electronic transition with the indirect state. Figure 12 reveals that the device can absorb most of the incident radiations.
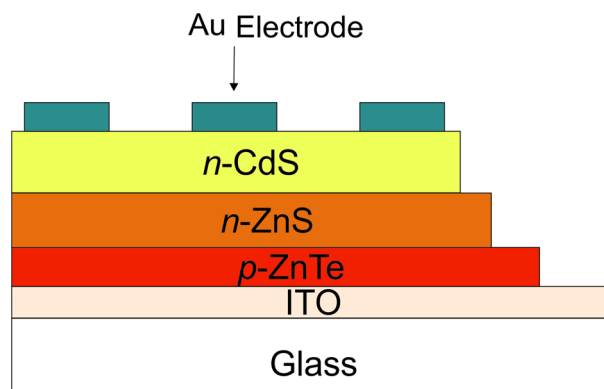

Fig. 11 Solar cell device structure diagram

2.1 Device performance

The thin-film-based solar cells consist of at least two kinds of semiconducting layers: a narrow bandgap absorber layer and a wide bandgap window layer. The most promising absorbing candidates for thin-film solar cell is a p-type CdTe ($E_g = 1.5$ eV) along with n-type CdS ($E_g = 2.42$ eV) that is usually used as a window layer. Recent works on multilayer-graded bandgap solar cells revealed high Voc (1 V) and excellent FF (0.80) values [12, 42, 59–66]. As discussed before, reducing the thickness of CdS layer (below 250 nm) is regularly done to minimize the recombination current caused by the absorption. Unfortunately, this reduction activates the pin-holes formation giving rise to creating unwanted shunting paths and consequently all solar cell

Fig. 12 Transmission spectra of Glass/ZnTe/ZnS/CdS multilayer thin-film
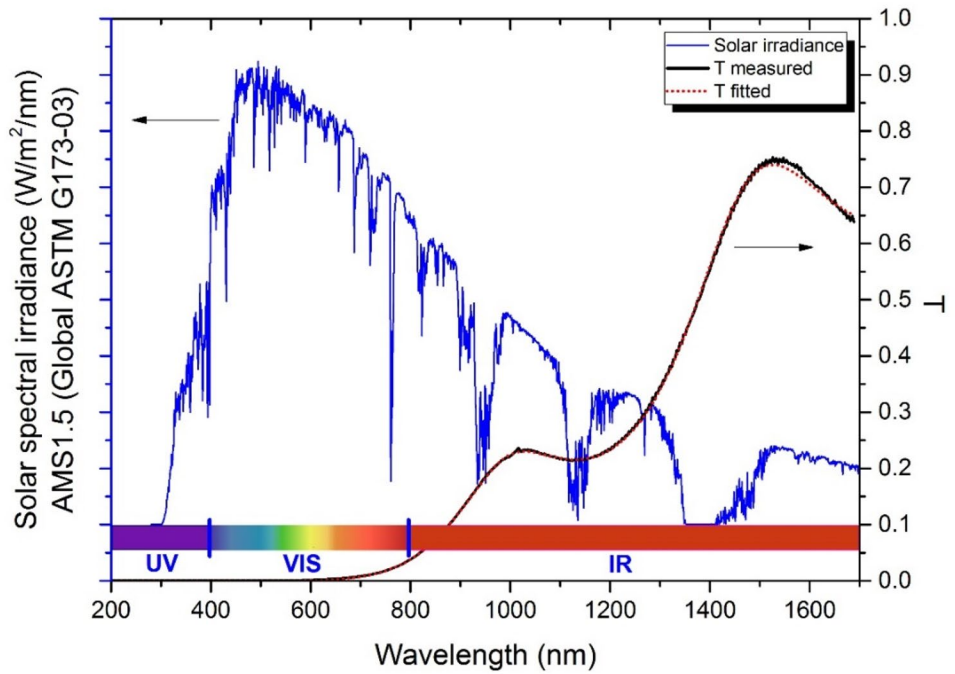
parameters including efficiency will be reduced. Here, we have fabricated 'PNN' type solar cell with structure glass/ITO/ZnTe/ZnS/CdS/Au. ZnS is used for two reasons: first, it works as buffer layer to prevent the diffusion of CdS into ZnTe layer during deposition. Second, the bandgap energy of ZnS is about 3.6 which is wider that the other two layers to assist in carrier's migration and reduce recombination and allows more photons with higher energy to pass through it. Therefore, engineering of bandgap energy will improve,

in principle, device performance. Figure 13 illustrates the energy band diagram for the device.

The optical properties of the device were investigated using ellipsometric measurements. Figure 14 shows the measured ellipsometric parameters for 'glass/ITO/ZnTe/ZnS/Cd' multilayer device. It is clear that the best fit was performed, this is very important to ensure that the obtaining results will be correct with accuracy. The deduced optical constants, n and k are illustrated in Fig. 15. From

Fig. 13 Energy band diagram for glass/ITO/ZnTe/ZnS/CdS/Au solar cell device
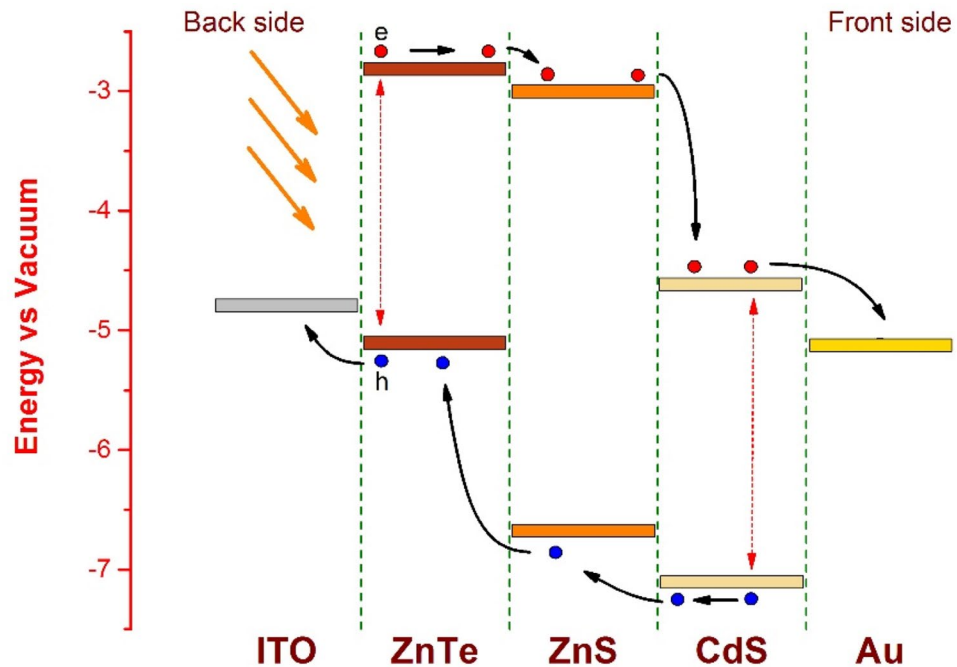
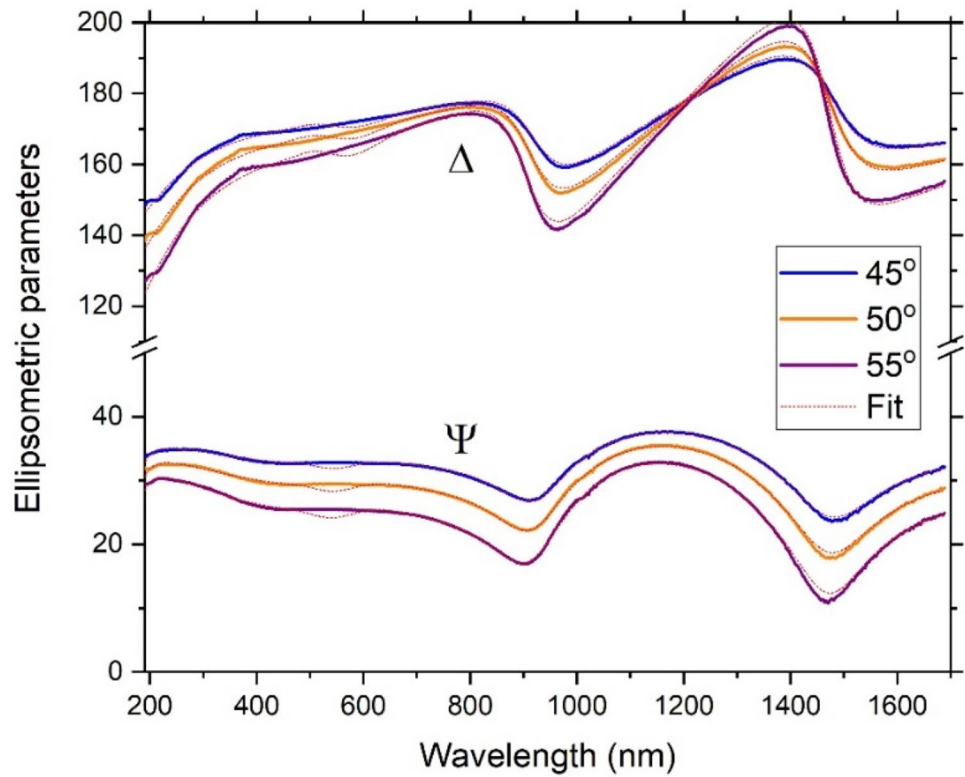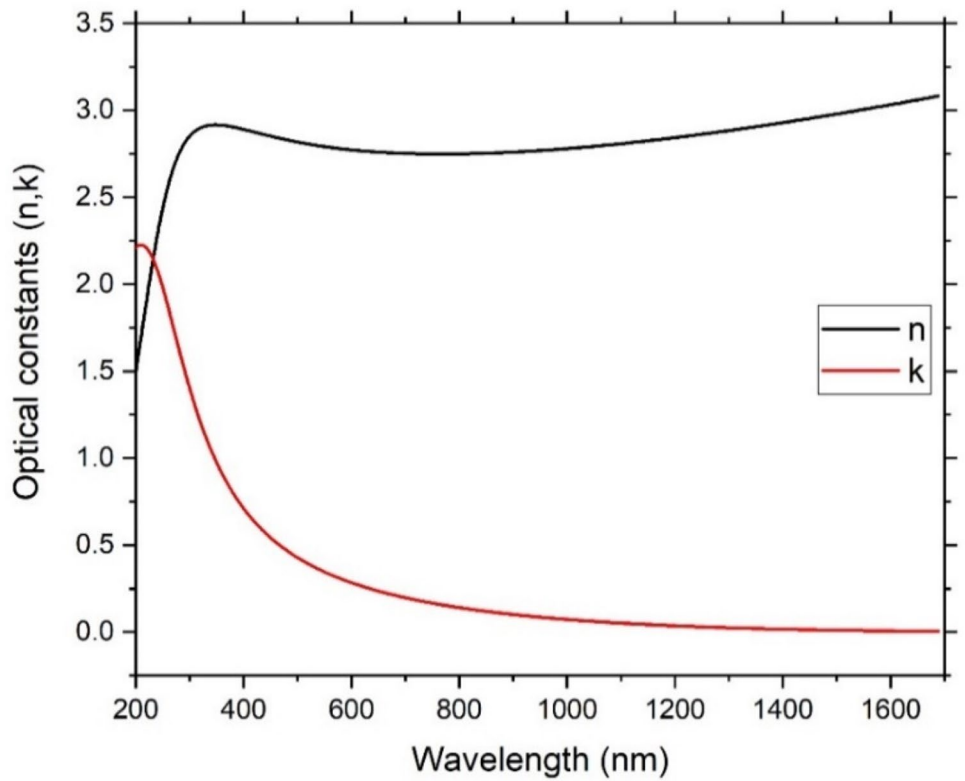**Fig. 14** Ellipsometric parameters for glass/ZnTe/ZnS/CdS multilayer thin-film

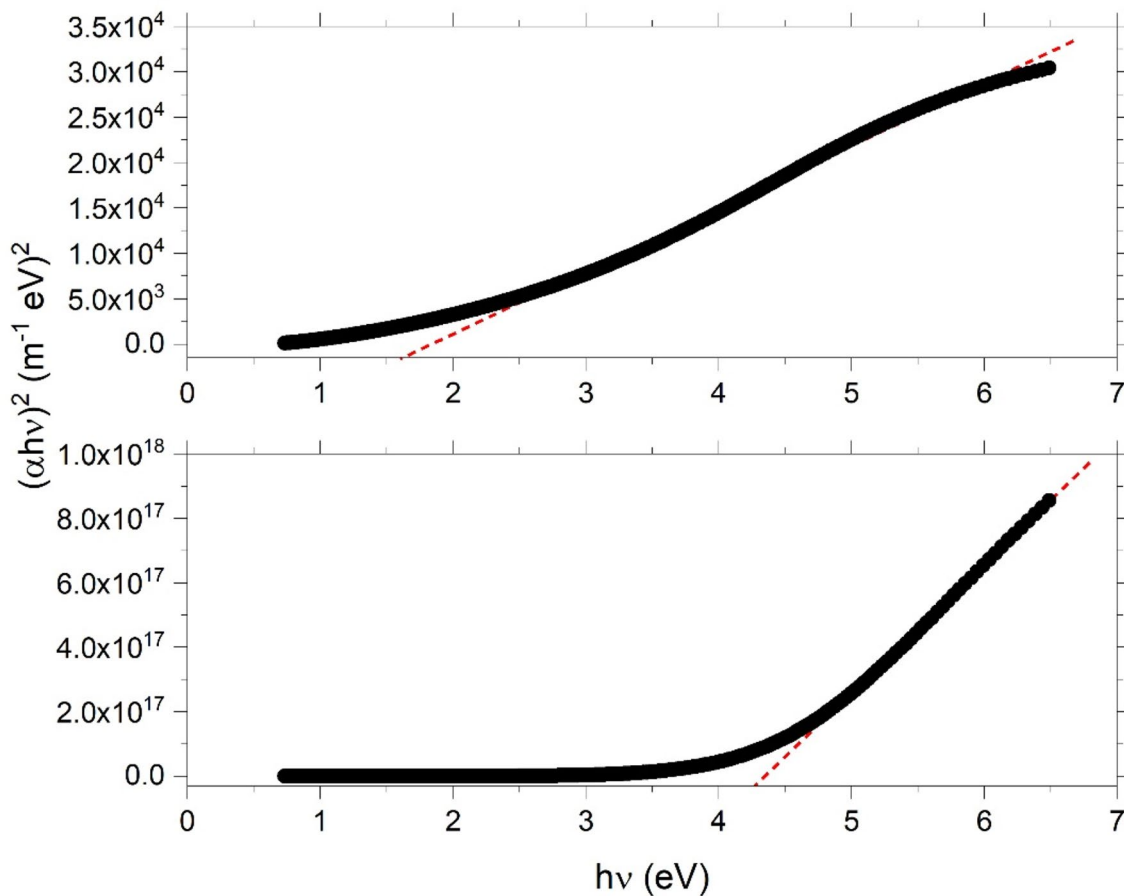**Fig. 15** Optical constants for glass/ZnTe/ZnS/CdS multilayer thin-film

Fig. 16 Tauc's plots for glass/ZnTe/ZnS/CdS multilayer thin-film

the calculated k values, the optical energy gaps of the device were also evaluated. Figure 16 presents the Tauc's plots of the device.

According to Tauc's analysis, the device shows two different types of optical energy gaps. The direct wide energy gap ($E_g = 4.2$ eV) will permit the device to absorb considerable part of IR radiation. The thermal energy from this radiation will assist the indirect transition ($E_g = 1.6$ eV) within the device. The value for the indirect bandgap is close to the optimal bandgap value of single-junction solar cell devices [67–72].

Figure 17 shows J–V characteristic curve of the fabricated solar cell device. This curve was measured with an active cell area of 0.09 cm^2 under Air Mass 1.5 solar irradiations with 100 mW/cm^2. From this curve, the cell's short-circuit current density (J_{sc}), open circuit voltage (V_{oc}), current density (J_{mpp}) and voltage (V_{mpp}) at the maximum power point were evaluated. Additionally, other cell parameters including, fill factor, series resistance, parallel resistance, and efficiency were also calculated. All calculated characteristics parameters are summarized in Table 2.

3 Conclusion

Nanoscale thin films of some important semiconductor materials, i.e., ZnTe, ZnS and CdS have been successfully prepared by e-beam evaporation technique. Structural investigations of the samples were performed by XRD analysis and the surface morphologies were investigated by AFM. Optical characterizations were performed by spectroscopic ellipsometry. Bandgap engineering for enhanced device performance with structure glass/ITO/ZnTe/ZnS/CdS/Au was established to assist charge carrier transfer and decrease recombination process. The fabricated solar cell was characterized by J–V measurements and all-important parameters were extracted. The value of the obtained efficiency is 16.5% indicating a promising result, especially as all the layers were very thin in comparison to the commercial solar cell devices. In fact, the total thickness of the whole device is below 1 μm. At present, the obtained efficiency can be further improved if the combinations of materials thickness and design structure are fully optimized. Some layers should be modified by doping with other elements to tune their energy gaps. Back metal electrode also required much attention to

Fig. 17 J–V characteristic curves for glass/ITO/ZnTe/ZnS/CdS/Au solar cell device
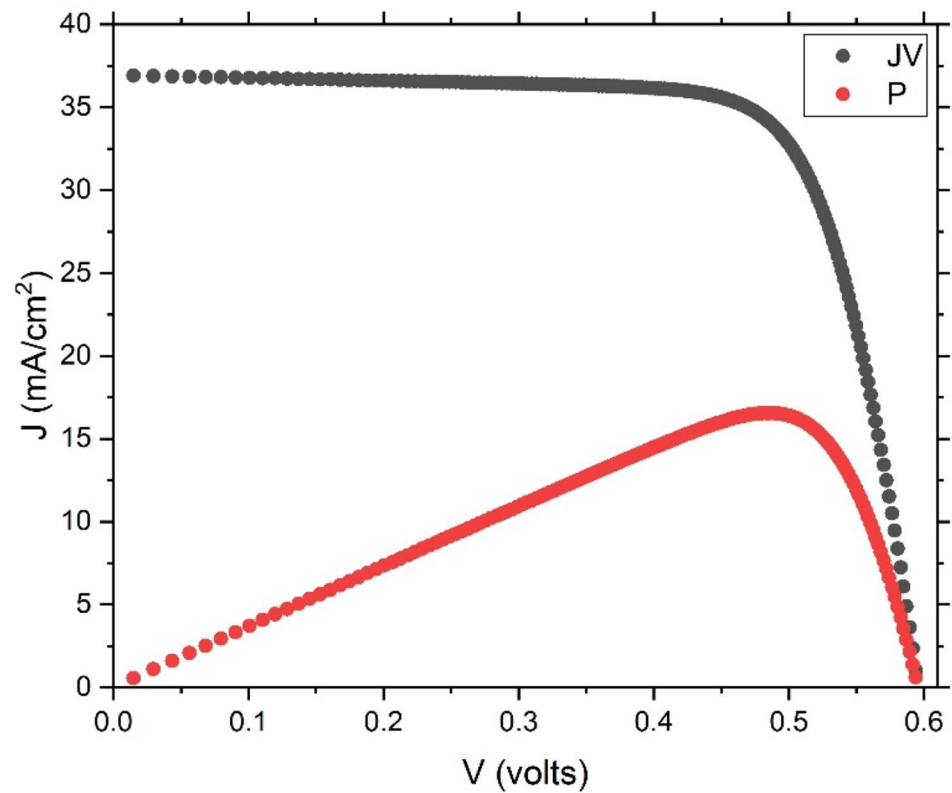

Table 2 Characteristic parameters for glass/ITO/ZnTe/ZnS/CdS/Au solar cell device

J_{sc} (mA/m^2)	V_{oc} (V)	J_{mpp} (mA/m^2)	V_{mpp} (V)	FF	R_s (Ω)	R_{shunt} (Ω)	Efficiency, η (%)
36.94	0.59	32.01	0.51	0.75	0.98	593	16.5

reduce contact resistance and enhance charge transfer and collection to external circuit.

Availability of data and material Not applicable.

Code availability Not applicable.

Compliance with ethical standards

Conflict of interest No conflict of interest.

References

1. R. Keshav, M.G. Mahesha, Optical and electrical characterization of vacuum deposited n-CdS/n-ZnS bilayers. Sol. Energy **167**, 172–178 (2018)

2. M. Samadpour, Efficient CdS/CdSe/ZnS quantum dot sensitized solar cells prepared by ZnS treatment from methanol solvent. Sol. Energy **144**, 63–70 (2017)

3. K.M. Deng, L. Li, CdS nanoscale photodetectos. Adv. Mater. **26**(17), 2619–2635 (2014)

4. X.S. Fang, L.M. Wu, L.F. Hu, ZnS nanostructure arrays: a developing material star. Adv. Mater. **23**(5), 585–598 (2011)

5. J.H. Kim et al., Raman spectroscopy of ZnS nanostructures. J. Raman Spectrosc. **43**(7), 906–910 (2012)

6. H.Q. Li et al., One-dimensional CdS nanostructures: a promising candidate for optoelectronics. Adv. Mater. **25**(22), 3017–3037 (2013)

7. T. Ling et al., Highly conductive CdS inverse opals for photochemical solar cells. Adv. Func. Mater. **24**(5), 707–715 (2014)

8. Y. Nandan, M.S. Mehata, Wavefunction engineering of type-I/type-II excitons of CdSe/CdS core-shell quantum dots. Sci. Rep. (2019). https://doi.org/10.1038/s41598-018-37676-3

9. N. Balis et al., Quantum dot sensitized solar cells based on an optimized combination of ZnS, CdS and CdSe with CoS and CuS counter electrodes. Electrochim. Acta **91**, 246–252 (2013)

10. Y.L. Chen et al., Enhanced solar cell efficiency and stability using ZnS passivation layer for CdS quantum-dot sensitized actinomorphic hexagonal columnar ZnO. Electrochim. Acta **118**, 176–181 (2014)

11. T. Tokuda, K. Yoshino, Growth and characterization of ZnS films by spray pyrolysis. Physica Status Solidi C Curr. Top. Solid State Phys. **10**(7–8), 1102–1106 (2013)

12. S. Ulicna et al., Development of ZnTe as a back contact material for thin film cadmium telluride solar cells. Vacuum **139**, 159–163 (2017)

13. Z. Li et al., Scalable fabrication of perovskite solar cells. Nat. Rev. Mater. **3**(4), 18017 (2018)

14. T. Leijtens et al., Opportunities and challenges for tandem solar cells using metal halide perovskite semiconductors. Nat. Energy **3**(10), 828–838 (2018)

15. L. Qiu et al., Scalable fabrication of metal halide Perovskite solar cells and modules. ACS Energy Lett. **4**(9), 2147–2167 (2019)

16. S. Almosni et al., Material challenges for solar cells in the twenty-first century: directions in emerging technologies. Sci. Technol. Adv. Mater. **19**(1), 336–369 (2018)

17. J. Li et al., Highly efficient thermally co-evaporated perovskite solar cells and mini-modules. Joule **4**(5), 1035–1053 (2020)

18. C.-G. Park et al., All-inorganic perovskite CsPbI$_2$Br through co-evaporation for planar heterojunction solar cells. Electron. Mater. Lett. **15**(1), 56–60 (2019)

19. E. Camacho-Espinosa et al., All-sputtered CdTe solar cell activated with a novel method. Sol. Energy **193**, 31–36 (2019)

20. Q. Tang, H. Yao, Efficiency enhancement of TiOx electron-transporting layer-based ultrathin p-type c-Si solar cell by reactive sputtering of backside MoOx hole-transporting contact. J. Mater. Sci.: Mater. Electron. **31**(8), 6406–6417 (2020)

21. W.-L. Chen, D.-H. Kuo, T.T.A. Tuan, Preparation of CuSbS$_2$ thin films by co-sputtering and solar cell devices with band gap-adjustable n-type InGaN as a substitute of ZnO. J. Electron. Mater. **45**(1), 688–694 (2016)

22. Q. Wang et al., One-step RF magnetron sputtering method for preparing Cu(In, Ga)Se$_2$ solar cells. J. Mater. Sci. Mater. Electron. **29**(14), 11755–11762 (2018)

23. Y. Zhang et al., Fabrication of 4.9% efficient Cu$_2$ZnSnS$_4$ solar cell using electron-beam evaporated CdS buffer layer. Thin Solid Films **685**, 145–150 (2019)

24. A.K.M. Hasan et al., Optoelectronic properties of electron beam-deposited NiOx thin films for solar cell application. Results Phys. **17**, 103122 (2020)

25. J. Jin et al., Efficient and stable perovskite solar cells through e-beam preparation of cerium doped TiO$_2$ electron transport layer, ultraviolet conversion layer CsPbBr$_3$ and the encapsulation layer Al2O$_3$. Sol. Energy **198**, 187–193 (2020)

26. J. Feng et al., E-beam evaporated Nb$_2$O$_5$ as an effective electron transport layer for large flexible perovskite solar cells. Nano Energy **36**, 1–8 (2017)

27. Z. Zhang et al., Electrodeposition of Cu thin film assisted by Cu nanoparticles for Cu$_2$ZnSnSe$_4$ solar cell applications. Appl. Phys. A **125**(9), 599 (2019)

28. S.Z. Werta, O.K. Echendu, F.B. Dejene, Physico-chemical studies of Cd$_{1-x}$Zn$_x$S thin films produced by simple two-electrode electrodeposition system for solar cell application. J. Mater. Sci. Mater. Electron. **30**(6), 6201–6211 (2019)

29. D.G. Diso et al., Optimisation of CdTe electrodeposition voltage for development of CdS/CdTe solar cells. J. Mater. Sci. Mater. Electron. **27**(12), 12464–12472 (2016)

30. A.A. Ojo, I.M. Dharmadasa, Progress in development of graded bandgap thin film solar cells with electroplated materials. J. Mater. Sci. Mater. Electron. **28**(9), 6359–6365 (2017)

31. R. Chandran, S.K. Panda, A. Mallik, A short review on the advancements in electroplating of CuInGaSe$_2$ thin films. Mater. Renew. Sustain. Energy **7**(2), 6 (2018)

32. A. Ekinci, Ö. Şahin, S. Horoz, Chemical bath deposition of Co-doped PbS thin films for solar cell application. J. Mater. Sci. Mater. Electron. **31**(2), 1210–1215 (2020)

33. A. Ashok et al., Comparative studies of CdS thin films by chemical bath deposition techniques as a buffer layer for solar cell applications. J. Mater. Sci. Mater. Electron. **31**(10), 7499–7518 (2020)

34. D. Lee et al., ZnS buffer layers grown by modified chemical bath deposition for CIGS Solar Cells. J. Electron. Mater. **47**(7), 3483–3489 (2018)

35. R.A. Awni et al., Influences of buffer material and fabrication atmosphere on the electrical properties of CdTe solar cells. Prog. Photovolt. **27**(12), 1115–1123 (2019)

36. J. Chantana et al., 22%-efficient Cd-free Cu(In, Ga)(S, Se) (2) solar cell by all-dry process using Zn$_{0.8}$Mg$_{0.2}$O and Zn$_{0.9}$Mg$_{0.1}$O:B as buffer and transparent conductive oxide layers. Prog. Photovolt. **28**, 79–89 (2019)

37. O.I. Olusola, M.L. Madugu, I.M. Dharmadasa, Investigating the electronic properties of multi-junction ZnS/CdS/CdTe graded bandgap solar cells. Mater. Chem. Phys. **191**, 145–150 (2017)

38. S.H. Hsu, S.F. Hung, S.H. Chien, CdS sensitized vertically aligned single crystal TiO$_2$ nanorods on transparent conducting glass with improved solar cell efficiency and stability using ZnS passivation layer. J. Power Sources **233**, 236–243 (2013)

39. H. Ferhati, F. Djeffal, Graded band-gap engineering for increased efficiency in CZTS solar cells. Opt. Mater. **76**, 393–399 (2018)

40. L.F. Teng et al., Novel two-step CdS deposition strategy to improve the performance of Cu$_2$ZnSn(S, Se)(4) solar cell. J. Energy Chem. **42**, 77–82 (2020)

41. K. Makita et al., III–V//Si multijunction solar cells with 30% efficiency using smart stack technology with Pd nanoparticle array. Prog. Photovolt. **28**, 16–24 (2019)

42. P.K. Nayak et al., Photovoltaic solar cell technologies: analysing the state of the art. Nat. Rev. Mater. **4**(4), 269–285 (2019)

43. F.H. Alharbi, S. Kais, Theoretical limits of photovoltaics efficiency and possible improvements by intuitive approaches learned from photosynthesis and quantum coherence. Renew. Sustain. Energy Rev. **43**, 1073–1089 (2015)

44. S.A. Pawar et al., Quantum dot sensitized solar cell based on TiO2/CdS/CdSe/ZnS heterostructure (vol 203, pg 74, 2016). Electrochim. Acta **211**, 1092–1092 (2016)

45. F. Khodam, A.R. Amani-Ghadim, S. Aber, Mg nanoparticles core-CdS QDs shell heterostructures with ZnS passivation layer for efficient quantum dot sensitized solar cell. Electrochim. Acta **308**, 25–34 (2019)

46. J.F. Han et al., Preparation and characterization of ZnS/CdS bi-layer for CdTe solar cell application. J. Phys. Chem. Solids **74**(12), 1879–1883 (2013)

47. I.O. Oladeji, L. Chow, Synthesis and processing of CdS/ZnS multilayer films for solar cell application. Thin Solid Films **474**(1–2), 77–83 (2005)

48. V. Hernandez-Calderon et al., Optimization of Cd$_x$Zn$_{1-x}$S compound from CdS/ZnS bi-layers deposited by chemical bath deposition for thin film solar cells application. Thin Solid Films **676**, 100–107 (2019)

49. H. Rojas-Chavez et al., ZnTe semiconductor nanoparticles: a chemical approach of the mechanochemical synthesis. Mater. Sci. Semicond. Process. **86**, 128–138 (2018)

50. A. Mayabadi et al., Electrochemical deposition of p-CdTe nanoparticle thin films for solar cell applications. J. Mater. Sci. Mater. Electron. **28**(24), 18745–18754 (2017)

51. Y. Ding et al., Nanoporous TiO$_2$ spheres with tailored textural properties: Controllable synthesis, formation mechanism, and photochemical applications. Prog. Mater Sci. **109**, 100620 (2020)

52. Z. Yuan, Fabrication, performance and atmospheric stability of inverted ZnO nanoparticle/polymer solar cell. Appl. Phys. A **118**(1), 75–81 (2015)

53. J.N. Hilfiker et al., Estimating depolarization with the jones matrix quality factor. Appl. Surf. Sci. **421**, 494–499 (2017)

54. J.N. Hilfiker et al., Spectroscopic ellipsometry characterization of multilayer optical coatings. Surf. Coat. Technol. **357**, 114–121 (2019)

55. J.N. Hilfiker et al., Survey of methods to characterize thin absorbing films with spectroscopic ellipsometry. Thin Solid Films **516**(22), 7979–7989 (2008)

56. J. Tauc, *Amorphous and Liquid Semiconductors*, vol. ix (Plenum, London, New York, 1974), p. 441

57. L. Brus, Size, dimensionality, and strong electron correlation in nanoscience. Acc. Chem. Res. **47**(10), 2951–2959 (2014)

58. L. Brus, Electronic wave functions in semiconductor clusters: experiment and theory. J. Phys. Chem. **90**(12), 2555–2560 (1986)

59. F. Ahmad, A. Lakhtakia, P.B. Monk, Optoelectronic optimization of graded-bandgap thin-film AlGaAs solar cells. Appl. Opt. **59**(4), 1018–1027 (2020)

60. D.A. Caselli, C.Z. Ning, High-performance laterally-arranged multiple-bandgap solar cells using spatially composition-graded $Cd_xPb_{1-x}S$ nanowires on a single substrate: a design study. Opt. Express **19**(Suppl 4), A686–A694 (2011)

61. O. Ergen et al., Graded bandgap perovskite solar cells. Nat. Mater. **16**(5), 522–525 (2017)

62. T.A.M. Fiducia et al., Understanding the role of selenium in defect passivation for highly efficient selenium-alloyed cadmium telluride solar cells (vol 4, pg 504, 2019). Nat. Energy **4**(6), 526–526 (2019)

63. C.A. Wolden et al., The roles of ZnTe buffer layers on CdTe solar cell performance. Sol. Energy Mater. Sol. Cells **147**, 203–210 (2016)

64. K.S. Lee et al., High power conversion efficiency of intermediate band photovoltaic solar cell based on Cr-doped ZnTe. Sol. Energy Mater. Sol. Cells **170**, 27–32 (2017)

65. P. Dingus et al., Low temperature growth and extrinsic doping of mono-crystalline and polycrystalline II–VI solar cells by MBE. Sol. Energy Mater. Sol. Cells **189**, 118–124 (2019)

66. W.K. Metzger et al., Exceeding 20% efficiency with in situ group V doping in polycrystalline CdTe solar cells. Nat. Energy **4**(10), 837–845 (2019)

67. F. Guo et al., A generic concept to overcome bandgap limitations for designing highly efficient multi-junction photovoltaic cells. Nat. Commun. **6**(1), 7730 (2015)

68. D.N. Micha, R.T. Silvares Junior, The influence of solar spectrum and concentration factor on the material choice and the efficiency of multijunction solar cells. Sci. Rep. **9**(1), 20055 (2019)

69. J.M. Ripalda, J. Buencuerpo, I. García, Solar cell designs by maximizing energy production based on machine learning clustering of spectral variations. Nat. Commun. **9**(1), 5126 (2018)

70. J.F. Geisz et al., Six-junction III–V solar cells with 47.1% conversion efficiency under 143 Suns concentration. Nat. Energy **5**(4), 326–335 (2020)

71. G. Jarosz, R. Marczyński, R. Signerski, Effect of band gap on power conversion efficiency of single-junction semiconductor photovoltaic cells under white light phosphor-based LED illumination. Mater. Sci. Semicond. Process. **107**, 104812 (2020)

72. A. Niv et al., Overcoming the bandgap limitation on solar cell materials. Appl. Phys. Lett. **100**(8), 083901 (2012)